



OPEN Research on noise-induced hearing loss based on functional and structural MRI using machine learning methods

Minghui Lv, Liping Wang, Ranran Huang, Aijie Wang, Yunxin Li & Guowei Zhang✉

Noise-induced hearing loss (NIHL) is a common occupational condition. The aim of this study was to develop a classification model for NIHL on the basis of both functional magnetic resonance imaging (fMRI) and structural magnetic resonance imaging (sMRI) by applying machine learning methods. fMRI indices such as the amplitude of low-frequency fluctuation (ALFF), fractional amplitude of low-frequency fluctuation (fALFF), regional homogeneity (ReHo), degree of centrality (DC), and sMRI indices such as gray matter volume (GMV), white matter volume (WMV), and cortical thickness were extracted from each brain region. The least absolute shrinkage and selection operator was used to reduce and select the optimal features. The support vector machine (SVM), random forest (RF) and logistic regression (LR) algorithms, were used to establish the classification model for NIHL. Finally, the SVM model based on combined fMRI indices, achieved the best performance, with area under the receiver operating characteristic curve of 0.97 and an accuracy of 95%. The SVM classification model that integrates fMRI indicators has the greatest potential for identifying NIHL patients and healthy people, revealing the complementary role of fMRI indicators in classification and indicating that it is necessary to include multiple indicators of the brain when establishing a classification model.

Keywords Noise-induced hearing loss, Functional magnetic resonance imaging, Structural magnetic resonance imaging, Machine learning

Noise-induced hearing loss (NIHL) is a hearing disorder caused by sensorineural hearing loss resulting from long-term exposure to occupational noise. NIHL is defined as long-term continuous exposure to unprotected environmental noise beyond the limits of national health standards. It typically presents as a progressive, high-frequency bilateral symmetrical sensorineural hearing loss. NIHL is the second most common occupational disease in the world after pneumoconiosis¹. While hearing loss caused by NIHL is irreversible, it is preventable. Studies^{2,3} have shown that early intervention is crucial for long-term protection. Therefore, early detection and diagnosis are particularly important.

Magnetic resonance imaging (MRI) is a noninvasive and reproducible imaging method for studying brain morphology and function. Functional magnetic resonance imaging (fMRI) can reflect baseline spontaneous neural activity associated with changes in brain function. Structural magnetic resonance imaging (sMRI) can reflect the anatomical structure of the brain. The development of MRI technology has made it possible for humans to explore and study the function and structure of the brain in detail.

Machine learning is an important research field in artificial intelligence. It has gradually become a powerful data analysis tool and has been used by an increasing number of researchers to study magnetic resonance data. Machine learning models have been widely used in the context of neuropsychiatric diseases and have demonstrated that alterations in brain function are highly important for distinguishing patients from healthy controls⁴. To construct a precise NIHL classification model, this paper introduces machine learning methods. The basic principle is that a model is trained by inputting a large amount of data, and the model learns the rules of the data and then classifies or predicts the newly input data. Studies⁵ have demonstrated that machine learning algorithms are potential tools for the prediction of noise-induced hearing impairment in workers exposed to diverse complex industrial noises. The support vector machine (SVM) is one of the most widely used machine learning models and has been used for classification modeling of hearing loss-related diseases^{6–8}. The random forest (RF)⁸ and logistic regression (LR)⁹ algorithms were also used. Three classification models for NIHL were established on the basis of the combination of MRI data and machine learning algorithms.

Imaging Department, Yantai Hospital, Yantai, China. ✉email: zhanggw0535@163.com

Specifically, the amplitude of low-frequency fluctuation (ALFF), fractional amplitude of low-frequency fluctuation (fALFF), regional homogeneity (ReHo) and degree of centrality (DC) were extracted from fMRI, and the gray matter volume (GMV), white matter volume (WMV) and cortical thickness were obtained from T1-weighted images. These MRI indicators were used because prior studies have successfully revealed alterations in ALFF^{10,11}, fALFF^{12,13}, ReHo¹⁴, DC¹⁵, GMV^{11,16}, WMV^{17,18} and cortical thickness¹⁹ in various brain regions of NIHL patients, such as the temporal, occipital and parietal lobes. Furthermore, indices derived from fMRI and sMRI are straightforward to calculate and analyze, thereby offering distinct benefits for clinical practice.

At present, there are no NIHL studies to determine which indicators can achieve the best classification performance with fMRI and sMRI data and whether multiple MRI index combinations can improve classification performance. Only a few studies have used MRI indicators to construct classification models for hearing loss patients²⁰, while other studies have used machine learning methods to predict hearing loss conditions^{8,9,21,22}. For example, in one study⁸, it was reported that the SVM model performed the best among the tested prediction models, with an accuracy of 75.36%. Li et al.²³ reported that the combination of sMRI and fMRI can be of added value in the construction of SVM classifiers to aid in the accurate identification of bipolar disorder in clinical settings.

Therefore, in this study, a classification model for NIHL patients based on fMRI and sMRI combined with machine learning methods was constructed. The main objectives were to investigate which MRI metric performs better and whether the combination of multiple MRI indices can improve classification performance. The aim of this study was to construct an NIHL classification model with good diagnostic efficiency and relatively stability, providing an image reference for clinical diagnosis. Therefore, this model could offer highly important insights for the prevention and early intervention of NIHL.

Materials and methods

Participants

In accordance with China's national occupational hygiene standards (GABZ 49-2014)²⁴, male patients diagnosed with NIHL at our hospital between 2014 and 2020 were selected. These individuals were of Han nationality and had education backgrounds ranging from primary school to university. Their mental status was normal (Mini-Mental State Examination (MMSE) score > 27), with no presence of neuropsychiatric disease. There were no systemic diseases or other factors that might affect brain structure or function. The personal information collection table, Hamilton Anxiety Scale (HAMA) and simple MMSE were used. Finally, the study included 66 NIHL patients and 66 age-, sex-, and education-matched healthy controls (HCs). Written informed consent was obtained from all participants after a full explanation of the procedures involved. This study protocol was approved by the Yantaishan Hospital Ethics Committee. The ethics approval number (2023014).

Statistical analysis

IBM SPSS26 software was used to analyze the data. Variables such as age, years of education, noise exposure time, HAMA score, MMSE score and other measurement data are presented as the mean \pm standard deviation. Independent sample t tests were performed to compare two groups, and $p < 0.05$ was considered statistically significant.

There were no significant differences in age, years of education or MMSE scores between the two groups (all $p > 0.05$), but there were significant differences in HAMA scores between the two groups ($p < 0.05$), it is shown in Table 1:

The flow chart of this study is shown in Fig. 1:

MRI acquisition

A GE Discovery MR 750 3.0 T scanner equipped with an 8-channel brain coil was used. All participants were in a supine position, with their eyes closed and ear plugs inserted to protect their hearing. The participants' heads were fixed. The T1-weighted 3D-FSPGR sequence parameters were as follows: repetition time (TR) of 6.9 ms, echo time (TE) of 3.4 ms, slice thickness of 1 mm, no septum, field of view (FOV) of 25.6 cm \times 25.6 cm, matrix size of 256 \times 256, excitation frequency of 1, and flip angle of 12°. The resting state fMRI (Rs-fMRI) echo planar imaging (EPI) parameters were as follows: TR of 2000 ms, TE of 35 ms, slice thickness of 4 mm, no gap, FOV of 24 cm \times 24 cm, matrix size of 64 \times 64, excitation number of 1, and flip angle of 90°.

Variable	HC	NIHL	<i>p</i> value
Age (years)	46.47 \pm 7.70	45.12 \pm 7.58	0.313
Education level (years)	10.85 \pm 2.23	10.41 \pm 1.73	0.209
Noise exposure time (years)	0	15.19 \pm 7.96	–
HAMA score	3.76 \pm 1.18	7.28 \pm 7.61	0.019
MMSE score	28.53 \pm 1.24	28.83 \pm 1.49	0.208

Table 1. Comparison of clinical data between NIHL patients and HCs (mean \pm standard deviation). HC, healthy control; NIHL, noise-induced hearing loss; HAMA, Hamilton Anxiety Scale; MMSE, Mini-Mental State Examination.

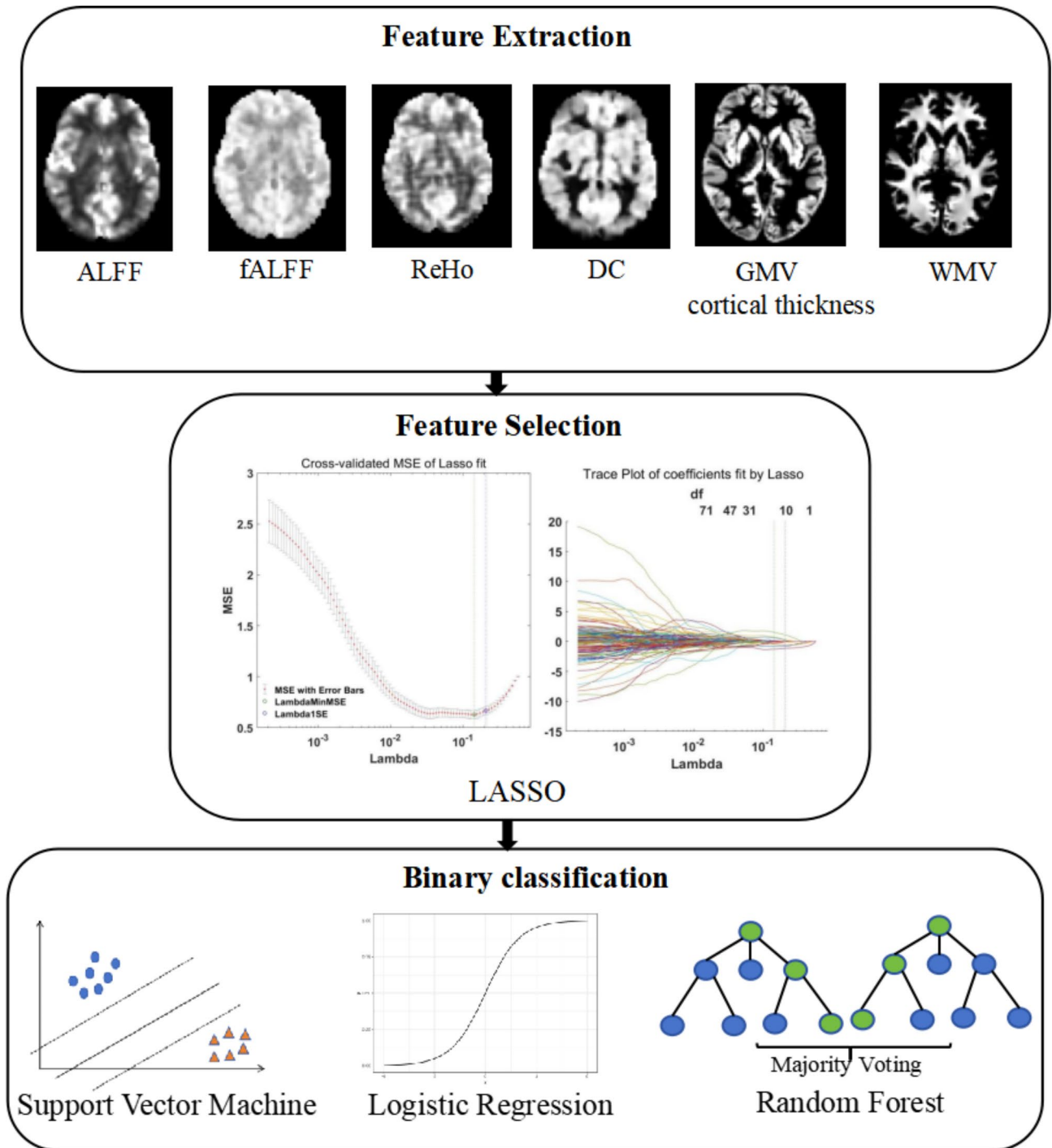


Fig. 1. Flow chart of this study. Feature extraction: fMRI included ALFF (amplitude of low-frequency fluctuation), fALFF (fractional amplitude of low-frequency fluctuation), ReHo (regional homogeneity), DC (degree of centrality); sMRI included GMV (gray matter volume), cortical thickness, WMV (white matter volume); A total of 360 fMRI and 328 sMRI features were extracted. The LASSO algorithm was subsequently used for feature selection. Three machine learning methods, the support vector machine (SVM), random forest (RF) and logistic regression (LR) algorithms, were used to establish a classification model for NIHL.

Functional data processing

Research on fMRI has revealed that the main indicators reflecting the activity of local brain regions include ALFF, fALFF, ReHo, and DC. The functional data were preprocessed via DPABI (<https://rfmri.org/DPABI>)²⁵ software. The preprocessing steps included the following: (1) conversion of DICOM file to NIfTI format; (2) removal of the first 10 time points; (3) slice-timing adjustment; (4) correction of head movement: data with head movement range > 2 mm or head rotation angle > 2° were excluded; (5) spatial normalization (the most widely

used DARTEL-based segmentation registration method was used, and the voxels were resampled to a size of $3 \times 3 \times 3 \text{ mm}^3$); (6) removal of covariates: the aim was to exclude the influence of mixed signals such as head movement, white matter, and cerebrospinal fluid (CSF) on the statistical results; (7) removal of linear drift: the linear drift of the signal caused by the heating of the magnetic resonance scanner during the image scanning process was removed; (8) filtering: the waveform of each voxel was bandpass filtered (0.01–0.08 Hz) in the time domain to reduce the physiological (breathing, heartbeat) noise interference at low and high frequencies; and (9) spatial smoothing: reducing the registration error, improving the signal-to-noise ratio and the normality of the data. A smoothing kernel with a size of 4 mm was used.

Following the initial data preprocessing and smoothing, mean ALFF and fALFF maps were generated. ALFF measures spontaneous low-frequency fluctuations within each voxel, while fALFF is the ratio of the ALFF signal of each voxel divided by the signal power in the whole frequency range. The ALFF/ALFF reflects the intensity of local brain activity. Following the initial data preprocessing and filtering, mean ReHo maps and mean weighted DC with a correlation threshold exceeding 0.25 were calculated and then smoothed with a Gaussian kernel of 4 mm. The ReHo measure quantifies the consistency of neural activity within a local neighborhood by calculating the Kendall coefficient of concordance (KCC) between a specific voxel and its neighboring voxels (27 voxels). Weighted DC, which represents the node strength, is defined as the sum of weights from edges connecting to a node. Through this process, we eventually obtained 90 ALFF, 90 fALFF, 90 ReHo and 90 weighted DC features by averaging all the voxels in each region of interest on the basis of the anatomical automatic labeling (AAL) template. Consequently, we extracted a total of 360 functional MRI features.

Structural data processing

The CAT12 toolbox (<https://neuro-jena.github.io/cat/>) in SPM12 (<https://www.fil.ion.ucl.ac.uk/spm/>) was used to preprocess the sMRI data with the following steps: the format of the image was converted; the tissue probability map template was used to segment the images into gray matter, white matter and cerebrospinal fluid; on the 1.5 mm isotropic adult brain template provided by CAT12, the DARTEL algorithm was used for registration and Montreal Neurological Institute (MNI) coordinate space normalization; the quality and homogeneity of the standardized images were checked; and a Gaussian kernel of 8 mm was used for further smoothing. Finally, the GMV, WMV and cortical thickness were extracted via CAT12, including 90 GMVs and 90 WMVs. Features were obtained via the AAL template, and 148 cortical thickness features were obtained via the Destrieux *aparc.a2009s* atlas²⁶. Consequently, we extracted a total of 328 sMRI features.

Feature selection

In data analysis and machine learning, feature selection is a key step that helps reduce model complexity, improve classification accuracy, and enhance model interpretability. Among the many feature selection methods, least absolute shrinkage and selection operator (LASSO) methods have attracted much attention because of their unique properties and wide application. LASSO regression was first proposed by Robert Tibshirani²⁷. In LASSO regression, a penalty term is added in the optimization of the objective function to introduce L1 regularization. The aim of L1 regularization is to achieve sparsity. Constraints can be imposed on some redundant variable coefficients to compress them 0. By selecting the nonzero coefficient corresponding characteristics, the features of the target variable that have the maximum predictive ability can be extracted to simplify the model and improve its generalizability.

In the model to be optimized, LASSO imposes constraints on the model coefficients through the penalty term formed by the L1 norm. The loss function to be optimized with constraints is as follows:

$$\arg \min_{\beta} \sum_{i=1}^N \left(y^i - \sum_{j=1}^{\rho} \beta_j x_j^i \right)^2 + \lambda \sum_{j=1}^{\rho} |\beta_j|, \quad (1)$$

where y^i is the class label of the i -th sample and N is the number of samples. x_j^i is the j -th feature of the i -th sample. β_j is the regression coefficient for the j -th feature and is a regularization parameter that determines the sparsity of the model. The larger λ is, the sparser the model; that is, the closer to 0 β_j is, the fewer features are selected. By selecting the features corresponding to nonzero coefficients, feature selection is realized.

In this study, the LASSO function in MATLAB was used for feature selection. When the minimum value of formula (1) is found, the mean squared error (MSE) is usually calculated and used to evaluate the model quality. To improve the classification accuracy, it is necessary to select the model corresponding to λ whose MSE is as small as possible. Tenfold cross-validation was used to select the optimal regularization parameter for the current model. The 'MSE' value represents the mean prediction squared error for each lambda value, as determined through cross-validation calculations. Figure 2 presents the cross-validation curve of the LASSO regression analysis. Two values of λ are generated in cross-validation: 'lambda.min' and 'lambda.1se'. Lambda.min is the best λ value that yields the minimum mean of the target parameter among all λ values, and lambda.1se is the λ value that yields the simplest model within the same variance range as that for lambda.min. After λ reaches a certain value, increasing the number of independent variables of the model, that is, reducing the λ value, cannot significantly improve the model performance. In this study, lambda.min is selected as the optimal λ because its penalty value is weaker than that for lambda.1se, which can contain enough eigenvalues. After obtaining the optimal λ value, the sparse coefficients corresponding to the optimal λ values are obtained, and the final eigenvalues are obtained by filtering the nonzero coefficients. Initially, the LASSO regression method was

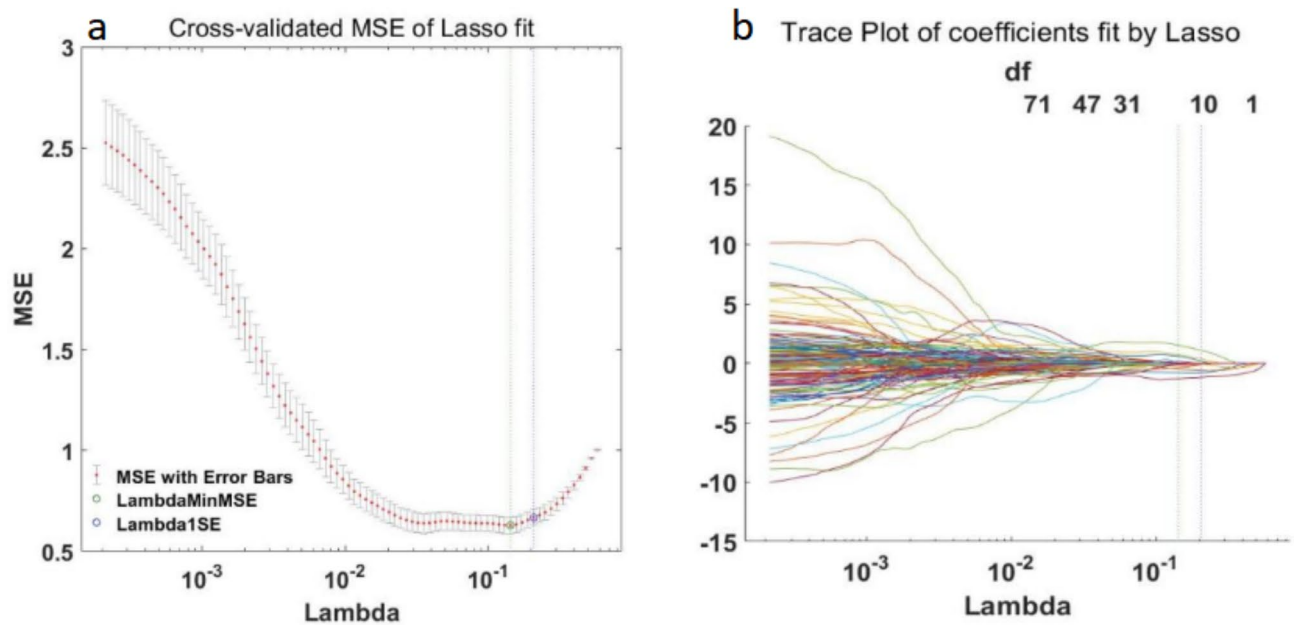


Fig. 2. Cross-validation curve of LASSO regression analysis. In figure a, the dashed line on the left side represents lambda.min, and the dashed line on the right side represents lambda.1se. In figure b, each curve represents the change trajectory of an independent variable coefficient, and the upper abscissa in the figure represents the number of nonzero coefficients in the model at this time.

employed to select the input features for single MRI index models. Then, LASSO dimensionality reduction was applied to the features selected by the sMRI and fMRI composite indices.

Machine learning algorithms

Support vector machine

The SVM, introduced by Cortes and Vapnik in 1990, operates by identifying a hyperplane that maximizes the margin between different classes to satisfy the classification requirements.

In addition, the good performance of the SVM requires the use of kernel functions, which allow high-dimensional data mapping to make the original high-dimensional data separable. The Gaussian kernel function was used in this study. Djemai et al.⁸ reported that an SVM based on the Gaussian kernel function has strong robustness and flexibility. Compared with other kernel functions, the RBF kernel function is more suitable for datasets with different characteristics. In this study, an SVM model with an RBF kernel was created on the basis of the LIBSVM²⁸ toolbox in MATLAB. Two important parameters are the penalty factor C and the kernel function γ . C is a regularization coefficient, which indicates the tolerance of the model to errors. γ is a hyperparameter of the radial basis function, which determines the distribution of the data after mapping to the new feature space. Grid search and cross-validation were used to find the optimal values for both C and γ . Various possible C and γ values were found via grid search, and then cross-validation was performed to find the C and γ values that yield the highest training accuracy. Then, the optimal parameters were applied to the training model, and the model performance index was obtained with the test set.

Logistic regression

LR is a widely used classification algorithm that solves binary classification problems. The rationale is divided into the following parts:

1. The core of logistic regression is to find a suitable predictor function. Usually, a linear function is chosen as the basis for the predictor function. Then, a sigmoid function is added. The sigmoid function can be used to map the output of a linear function between 0 and 1, resulting in a value that indicates the probability of a sample belonging to a certain class.

Sigmoid function:

$$g(z) = \frac{1}{1 + e^{-z}}, \quad (2)$$

Prediction function:

$$h_{\theta}(x) = g(\theta^T x) = \frac{1}{1 + e^{-\theta^T x}}, \quad (3)$$

The value of $h(x)$ is the probability that the result is 1. Therefore, for an input x , the probability of classifying it as class 1 or class 0 is as follows:

$$\begin{aligned} P(y = 1|x; \theta) &= h_{\theta}(x) \\ P(y = 0|x; \theta) &= 1 - h_{\theta}(x), \end{aligned} \quad (4)$$

2. The cost function is a measure of the deviation between the output of the prediction function and the class of the training data. It is usually derived on the basis of maximum likelihood estimation.

$$\text{Cost}(h_{\theta}(x), y) = \begin{cases} -\log(h_{\theta}(x)) \\ -\log(1 - h_{\theta}(x)) \end{cases}, \quad (5)$$

The cost function can be expressed as the cross-entropy of the training data class y to the predicted output h , i.e.,

$$\begin{aligned} J(\theta) &= \frac{1}{m} \sum_{i=1}^m \text{Cost}(h_{\theta}(x^{(i)}), y^{(i)}) \\ &= -\frac{1}{m} \left[\sum_{i=1}^m y^{(i)} \log h_{\theta}(x^{(i)}) + (1 - y^{(i)}) \log(1 - h_{\theta}(x^{(i)})) \right], \end{aligned} \quad (6)$$

A smaller $J(\theta)$ value indicates a more accurate prediction function.

3. To find the optimal model parameters, the cost function needs to be minimized. In this study, the gradient descent algorithm was used to solve θ . In the gradient descent method, θ is updated in the opposite direction of the gradient of the cost function at each iteration until the cost function reaches its minimum value.

Random forest algorithm

The RF algorithm, which is an ensemble learning algorithm, was proposed by Breiman et al.²⁹. By constructing multiple decision trees and combining them, more stable and accurate prediction results can be obtained. In a random forest, each decision tree is constructed by randomly selecting samples and features; this randomness reduces the overfitting of the decision tree to the training data and improves the generalizability of the model. For the classification problem, the random forest algorithm determines the final prediction result by voting.

Performance indices

In medical diagnosis, the accuracy rate and recall rate are usually used to evaluate the classifier quality. Accuracy reflects the proportion of instances that are accurately categorized in relation to the entire set of instances within a specified test collection. Recall, also known as sensitivity, is the ratio of samples that were actually positive and were predicted to be positive to samples that were actually positive. Specificity indicates the proportion of samples that are correctly identified as negative among those that are actually negative.

$$\text{Accuracy : } ACC = \frac{TP + TN}{TP + TN + FP + FN} \quad (7)$$

$$\text{Sensitivity : } Sens = \frac{TP}{TP + FN} \quad (8)$$

$$\text{Specificity : } Spec = \frac{TN}{FP + TN} \quad (9)$$

Note: TP: True Positive; TN: True Negative; FP: False Positive; FN: False Negative;

The receiver operating characteristic (ROC) curve also reflects the performance of different classification algorithms. The vertical axis represents the true positive rate (TPR), which is also sensitive, and the horizontal axis represents the false-positive rate (FPR). The closer to the vertical axis the ROC curve is, the better the model prediction. The larger the area under the receiver operating characteristic (AUROC) curve is, the better the performance of the algorithm.

Results

LASSO feature selection

Figure 3 shows the LASSO regression analysis cross-validation curve. The numbers of features selected by ALFF, fALFF, ReHo, DC, cortical thickness, GMV, and WMV were 19, 33, 27, 21, 12, and 3, respectively. The number of features selected by combined fMRI was 42, including 15 ALFF, 7 fALFF, 15 ReHo, and 5 DC features. The number of features selected by combined sMRI was 25, including 4 GMV, 4 WMV, and 17 cortical thickness features. The number of features selected by the combined fMRI and sMRI was 14, which included 6 ALFF, 7 ReHo, and 1 cortical thickness features.

Classifier performance for MRI indices alone

Table 2 shows the performance values of the AUC, accuracy, sensitivity, and specificity of single MRI indices in the SVM, LR, and RF classification models. Figure 4 shows the ROC curves of the individual indicators in the three classification models. On the basis of a single MRI index, the SVM model for ReHo performed best, with

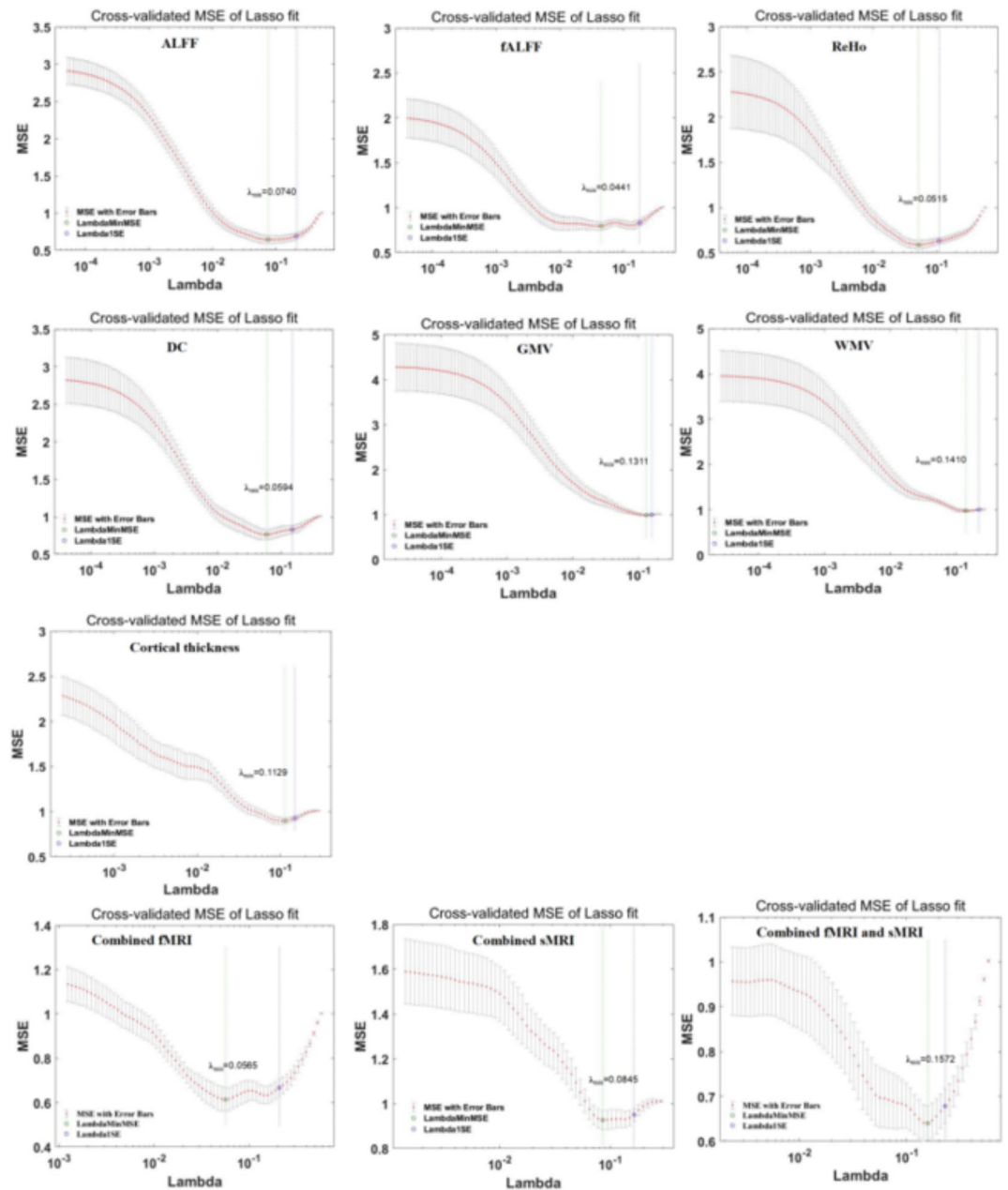


Fig. 3. LASSO selection of the optimal lambda value through cross-validation. *Notes:* ALFF, amplitude of low-frequency fluctuation; fALFF, fractional amplitude of low-frequency fluctuation; ReHo, regional homogeneity; DC, degree of centrality; GMV, gray matter volume; WMV, white matter volume; fMRI, functional magnetic resonance imaging; and sMRI, structural magnetic resonance imaging. The longitudinal coordinate represents the binomial deviation. The dashed line on the left represents lambda.min, and the dashed line on the right represents lambda.1se.

an AUC of 0.94 and an accuracy of 88%. Good performance was also noted using the SVM model with ALFF, with an AUC of 0.93 and an accuracy of 89%. The performance of the GMV and WMV classification models was poor.

Classifier performance for combined MRI indices

Table 3 shows the performance values of the AUC, accuracy, sensitivity, and specificity of the combined MRI indicators for the SVM, LR, and RF classification models. Figure 5 shows the ROC curves of the combined MRI indicators for the three classification models, among which the SVM model of the comprehensive fMRI indicators performed best, with an AUC of 0.97 and an accuracy of 95%. A Delong test was applied to compare ROC curve performance of the three models, and it was found that there were significant differences between SVM and RF and between SVM and LR (SVM vs. RF and SVM vs. LR: $p < 0.05$).

Model	Indices	AUC	Acc	Sens	Spec
SVM	ALFF	0.93	0.89	0.91	0.87
	fALFF	0.88	0.83	0.81	0.84
	ReHo	0.94	0.88	0.86	0.90
	DC	0.88	0.84	0.82	0.86
	GMV	0.65	0.65	0.71	0.59
	WMV	0.65	0.68	0.78	0.59
	Cortical thickness	0.82	0.79	0.77	0.80
RF	ALFF	0.92	0.84	0.78	0.91
	fALFF	0.71	0.73	0.72	0.75
	ReHo	0.90	0.84	0.88	0.82
	DC	0.75	0.77	0.85	0.69
	GMV	0.58	0.65	0.57	0.75
	WMV	0.66	0.69	0.69	0.69
	Cortical thickness	0.79	0.77	0.85	0.69
LR	ALFF	0.92	0.84	0.73	1.0
	fALFF	0.70	0.53	0.66	0.50
	ReHo	0.93	0.88	0.77	0.82
	DC	0.75	0.56	0.84	0.42
	GMV	0.52	0.58	0.62	0.50
	WMV	0.63	0.61	0.61	0.61
	Cortical thickness	0.72	0.56	0.50	0.66

Table 2. Performance of classification models on the basis of a single MRI index. AUC, area under the curve; Acc, accuracy; Sens, sensitivity; Spec, specificity. ALFF, amplitude of low-frequency fluctuation; fALFF, fractional amplitude of low-frequency fluctuation; ReHo, regional homogeneity; DC, degree of centrality; GMV, gray matter volume; WMV, white matter volume; SVM, support vector machine; RF, random forest; LR, logistic regression;

The combined fMRI indices lead to the extraction of 42 feature values through LASSO regression analysis. According to the coefficients of the selected variables, the most important features for the prediction of the target variable can be understood. The greater the absolute value of the coefficient is, the greater the influence of the variable on the response variable, that is, the greater the contribution to the classification model. The top 10 contributors were the ALFF of the right fusiform gyrus (FFG. R), fALFF of the left middle temporal gyrus (TPOmid. L), ReHo of the left insula (INS. L), ReHo of the left median cingulate and paracingulate gyri (DCG. L), ALFF of the right superior parietal gyrus (SPG. R), fALFF of the left inferior frontal gyrus (IFGoperc. L), ReHo of the left superior frontal gyrus (SFGmed. L), fALFF of the right superior occipital gyrus (SOG. R), ReHo of the right middle occipital gyrus (MOG. R), and ReHo of the right fusiform gyrus (FFG.R).

The middle 20 regions included the ReHo of the left inferior occipital gyrus (IOG. L), ReHo of the left middle frontal gyrus (MFG. L), fALFF of the right parahippocampal gyrus (PHG. R), ReHo of the left superior frontal gyrus (SFGdor. L), and ReHo of the right insula (INS. R), DC of the left temporal pole (TPOsup. L), ALFF in the right cuneus (CUN. R), ReHo of the left postcentral gyrus (PoCG. L), left postcentral gyrus (CAU. L), right inferior parietal (IPL. R), ALFF of the left temporal pole (TPOmid. L), fALFF values in the right supplementary motor area (SMA. R) and right inferior parietal (IPL. R), ALFF of the left inferior parietal (IPL. L), left fusiform gyrus (FFG. L), left postcentral gyrus (PoCG. L), ReHo of the right lenticular nucleus (PUT. R), ALFF of the temporal pole (TPOsup. L), DC of the right Rolandic operculum (ROL.R).

The other 12 brain areas included the ALFF of the left temporal pole (TPOmid. R), fALFF of right supplementary motor area (SMA. R), right inferior parietal (IPL. R), ALFF of the left inferior parietal (IPL. R), left fusiform gyrus (FFG. L), left postcentral gyrus (PoCG. L), ReHo of the right lenticular nucleus, putamen (PUT. R), ALFF of the temporal pole: superior temporal gyrus (TPOsup. L/R), DC of the right Rolandic operculum (ROL. R), and ReHo of the left angular gyrus (ANG. L), ALFF in the left cuneus (CUN. L), left inferior frontal gyrus (IFGoperc. L), and ReHo of the right hippocampus (HIP. R), ALFF in the left precuneus (PCUN. L), left caudate nucleus (CAU. L), the DC of the left lenticular nucleus, the pallidum (PAL. L), left superior frontal gyrus, medial (SFGmed. L), right fusiform gyrus (FFG. R), ALFF of the left supramarginal gyrus (SMG. L), fALFF of the right gyrus rectus (REC. R), and ALFF in the left angular gyrus (ANG.L). We found that the consistently selected brain regions in the ALFF, fALFF, ReHo, DC and combined fMRI data were the fusiform gyrus (FFG), superior parietal gyrus (SPG) and precuneus (PCUN).

Owing to the large number of selected feature values, we only show the regions of the top 20 features in the brain, as shown in Fig. 6 for details. Figure 7 shows the contribution values of these features to the classification model calculated via LASSO regression.

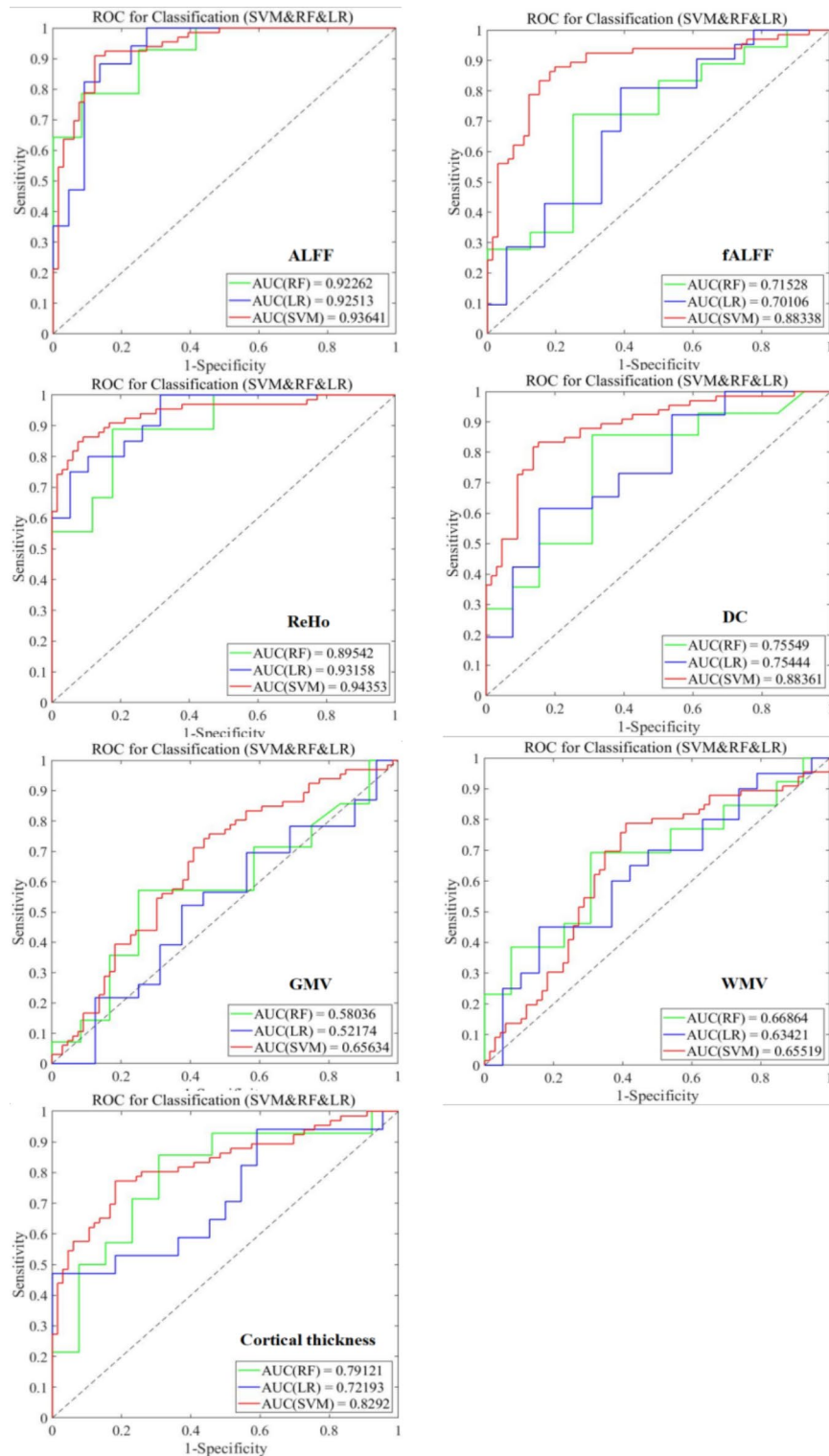


Fig. 4. ROC curves of classification models based on a single MRI index. *Notes:* ALFF, amplitude of low-frequency fluctuation; fALFF, fractional amplitude of low-frequency fluctuation; ReHo, regional homogeneity; DC, degree of centrality; GMV, gray matter volume; WMV, white matter volume; AUC, area under the curve; RF, random forest; LR, logistic regression; SVM, support vector machine.

Model	Indices	AUC	Acc	Sens	Spec
SVM	fMRI	0.97	0.95	0.96	0.93
	sMRI	0.84	0.82	0.78	0.84
	fMRI + sMRI	0.92	0.89	0.87	0.90
RF	fMRI	0.93	0.88	0.90	0.86
	sMRI	0.80	0.77	0.71	0.84
	fMRI + sMRI	0.85	0.80	0.71	0.91
LR	fMRI	0.95	0.89	0.95	0.84
	sMRI	0.76	0.66	0.63	0.70
	fMRI + sMRI	0.91	0.84	0.78	0.90

Table 3. Performance of classification models based on the combined MRI index. AUC, area under the curve; Acc, accuracy; Sens, sensitivity; Spec, specificity; SVM, support vector machine; RF, random forest; LR, logistic regression; fMRI, functional magnetic resonance imaging; sMRI, structural magnetic resonance imaging; fMRI indices included ALFF, fALFF, ReHo and DC; sMRI indices included GWV, WMV, and cortical thickness; and fMRI + sMRI indices included ALFF, fALFF, ReHo, DC, GWV, WMV, and cortical thickness.

Discussion

This study introduces machine learning with the combination of multiple MRI indices to distinguish NIHL patients from healthy controls. We used three different classifiers, SVM, RF, and LR, to construct a classification model. The SVM model, which integrates various fMRI metrics, such as ALFF, fALFF, ReHo and DC, demonstrated superior classification efficacy.

When considering individual MRI indices, the ReHo metric, which is utilized within an SVM classification framework, demonstrated superior efficacy, whereas the ALFF index also yielded creditable results. ReHo is a resilient computational technique that enables the quantification of the resting-state local synchronization of adjacent voxels, offering valuable insights into the uniformity of neural activity across the entire brain³⁰. Studies³⁰ have shown that abnormal changes in ReHo provide diagnostic value for neuroimaging biomarkers related to sudden sensorineural hearing loss disease. Wei Xinru et al.³¹ constructed a deep learning classification model for the auxiliary diagnosis of bipolar disorder and reported that ReHo had greater sensitivity in capturing differences in image features and that fMRI data based on ReHo could improve the performance of the classification model to a certain extent. The classification models do not perform well for GMV and WMV. However, research on the combination of sMRI data and machine learning methods to construct noise-based deafness prediction models is scarce. Considering the results of this study, the efficacy of employing a singular sMRI index for differentiating between individuals with NIHL and those without such data requires additional validation.

As expected, the classification model in which the combination of multilevel fMRI indices was implemented performed better than the single MRI index did. ALFF, fALFF, ReHo, and DC each provide unique insights into the neuroimaging alterations associated with NIHL. ALFF reflects the intensity of regional spontaneous brain activity³²; fALFF reflects the relative contribution of the oscillations³²; ReHo represents local coherence of spontaneous brain activity³³; and weighted DC shows the functional connectivity strength of a certain brain region to the whole brain³⁴. Furthermore, integrating various MRI indices at different levels clearly enhances the efficacy of classification models. This finding indicates a complementary effect of ALFF, fALFF, ReHo and DC on the classification of NIHL patients and HCs.

In this investigation, SVM demonstrated better performance than the LR and RF classifiers did, achieving notably elevated accuracy rates. This finding is consistent with previous research, Huang, FF. et al.³⁵ used MRI indices to discriminate patients with obsessive-compulsive disorder from HCs and reported that the SVM model with combined fMRI indices had the greatest potential to discriminate patients with obsessive-compulsive disorder from HCs. The superiority of the SVM method may be due to its ability to solve small-sample, high-dimensional problems³⁶. Abu Bakar et al.⁶ conducted a study on the importance of machine learning in hearing impairment and analyzed machine learning technology related to hearing assessment over the past 13 years. The SVM classifier outperformed other methods, with an accuracy of over 80%, and was recognized as the best-suited model within the field of auditory research.

Within the SVM framework, which integrates multiple fMRI indices, the features included the visual network (such as the fusiform gyrus, superior occipital gyrus, middle occipital gyrus, and cuneus), frontal parietal network (middle frontal gyrus, inferior frontal gyrus, etc.), and attention network (thalamus, medial and lateral cingulate gyrus, and dorsal-lateral superior frontal gyrus). These features include several auditory brain regions, such as the temporal pole: superior temporal gyrus and temporal pole: middle temporal gyrus, which is consistent with the findings of previous studies^{2,4,37}. Wu et al.⁴ combined static and dynamic neuroimaging features to distinguish sensorineural hearing impairment, and the selected brain regions after feature selection included auditory and non-auditory regions, such as temporal pole: superior temporal gyrus, precuneus and the superior parietal gyrus. Chen et al.¹² investigated the functional brain changes associated with sudden sensorineural hearing loss (SSNHL) using fMRI. They found that the primary regions exhibiting changes due to SSNHL are located in the auditory and visual cortices, as well as the precuneus. Li et al.⁴⁰ discovered that in the static fALFF, there is a significant decrease in the fusiform gyrus of patients with sudden sensorineural hearing loss. The consistent brain region in single fMRI measurements is the precuneus, which belongs to the parietal lobe and is involved in visual processing²; the fusiform gyrus is a part of the visual association cortex that is involved mainly

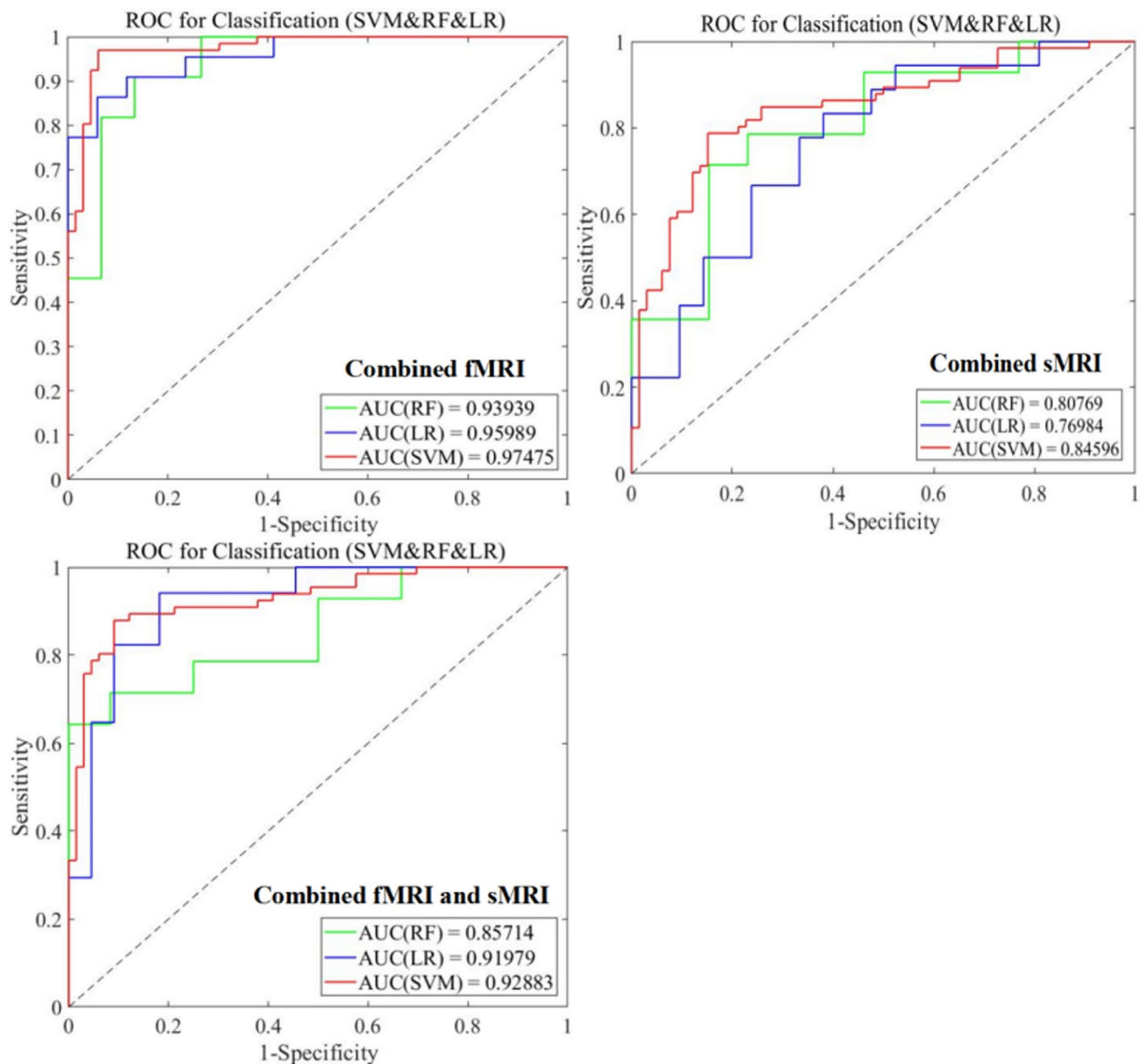


Fig. 5. ROC curves of classification models based on combined MRI indices. *Notes:* AUC, area under the curve; RF, random forest; LR, logistic regression; SVM, support vector machine; fMRI, functional magnetic resonance imaging; sMRI, structural magnetic resonance imaging; combined fMRI indices included ALFF, fALFF, ReHo and DC; combined sMRI indices included GWV, WMV, and cortical thickness; and combined fMRI and sMRI indices included ALFF, fALFF, ReHo, DC, GWV, WMV, and cortical thickness.

in the processing of visual speech³⁸; and the superior parietal gyrus is responsible mainly for processing higher-level cognitive functions, such as sensory integration and visuospatial processing, and plays an important role in cognitive and motor-related processes³⁹. Some studies^{39–42} have suggested that auditory deprivation may lead to functional reorganization of the auditory cortex and may enhance the interaction between auditory and visual brain areas. There is cross-modal reorganization of brain regions associated with hearing loss. Studies⁴³ have shown that hearing impairment is associated with alterations in resting-state brain organization, and effects have been shown in attention and cognitive control networks, as well as visual and sensorimotor regions. Hearing loss affects both auditory and nonauditory brain regions. The results of this study suggest that the role of each brain area index should be comprehensively considered in future research and that the neurophysiological mechanism of noise-induced hearing loss should be further explored.

There are several limitations in our study. For example, the sample size of this study was relatively small, and for machine learning research, the effect will be more stable with a larger sample size. This study involved only single-center data. Thus, more multicenter data need to be included to verify the practicality and stability of the model.

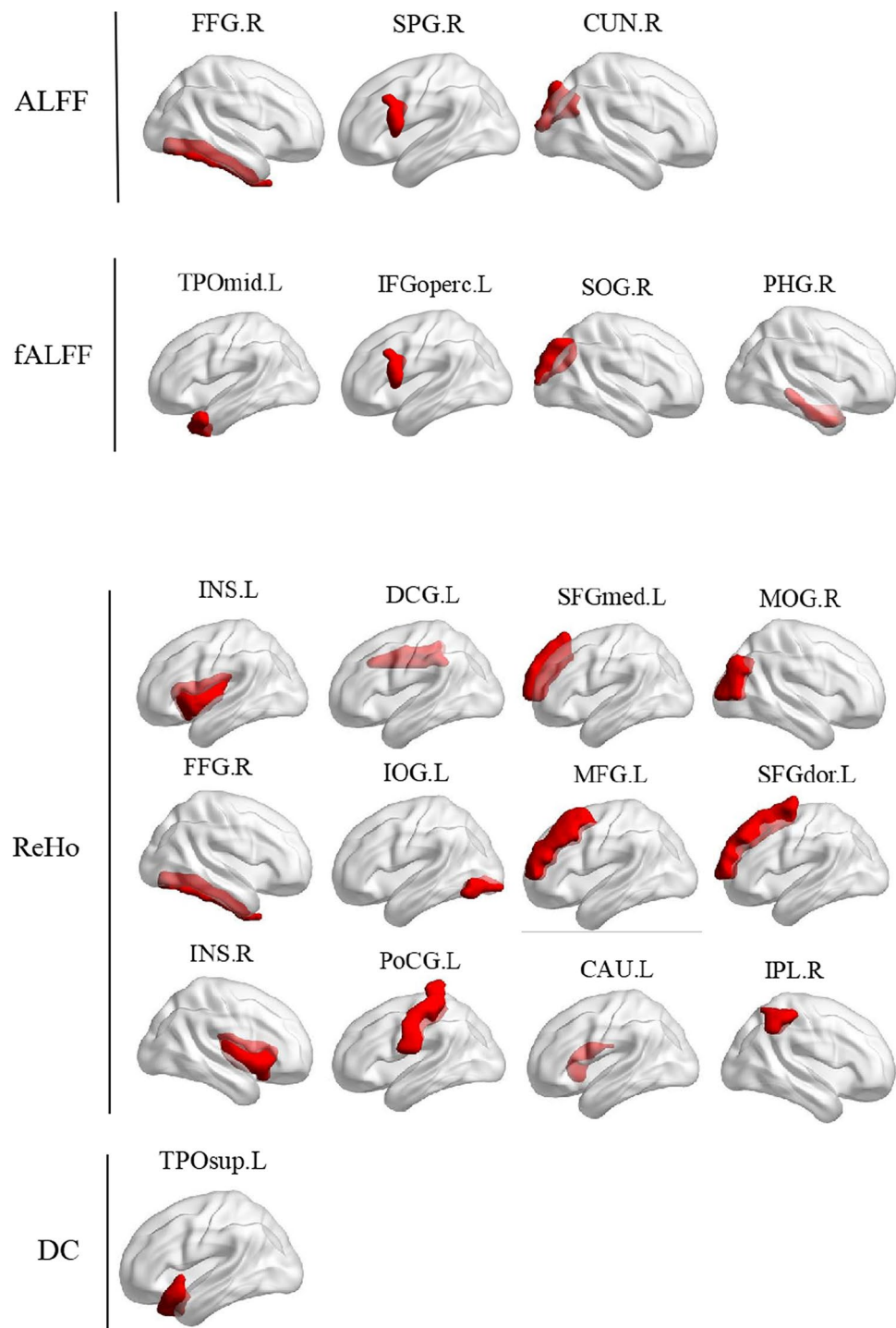


Fig. 6. Features of the contribution value for the top 20 included features in the combined fMRI indices. *Notes:* ALFF, amplitude of low-frequency fluctuation; fALFF, fractional amplitude of low-frequency fluctuation; ReHo, regional homogeneity; DC, degree of centrality.

In summary, the SVM model of combined fMRI indices, including ALFF, fALFF, ReHo and DC, exhibited good performance in discriminating NIHL patients from HCs. In future research, more feature combinations and algorithm optimization can be explored to further improve the classification accuracy and practicability.

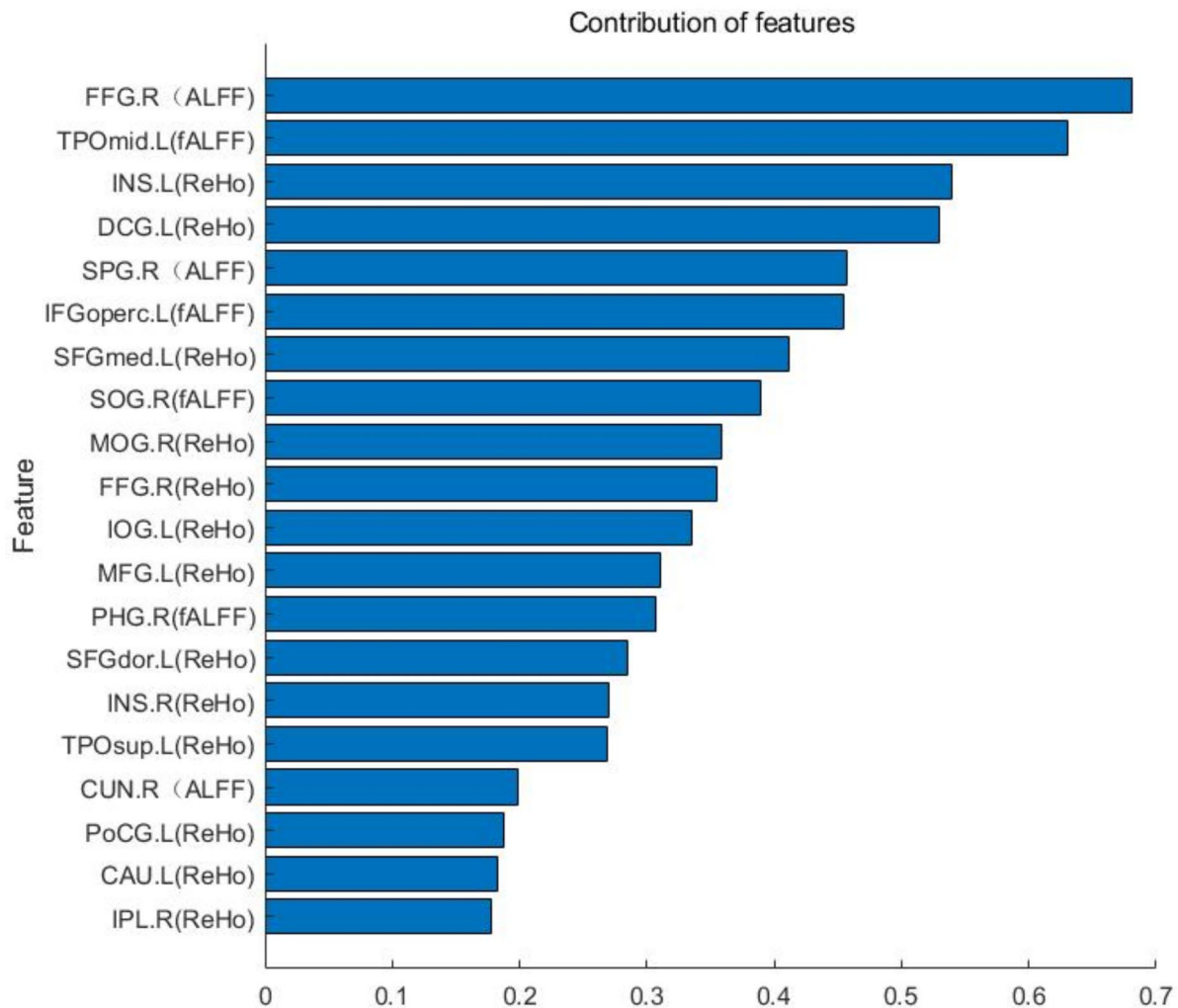


Fig. 7. The contribution of the top 20 features with combined fMRI indices. *Notes:* ALFF, amplitude of low-frequency fluctuation; fALFF, fractional amplitude of low-frequency fluctuation; ReHo, regional homogeneity; DC, degree of centrality.

Data availability

The datasets generated and analysed during the current study are not publicly available due to privacy or ethical restrictions but are available from the corresponding author on reasonable request.

Received: 26 July 2024; Accepted: 16 January 2025

Published online: 26 January 2025

References

- Liu, C. et al. The Burden of occupational noise-induced hearing loss from 1990 to 2019: An analysis of global burden of disease data. *Ear Hearing* <https://doi.org/10.1097/AUD.0000000000001505> (2024).
- Ma, X. et al. Intrinsic network changes associated with cognitive impairment in patients with hearing loss and tinnitus: A resting-state functional magnetic resonance imaging study. *Ann. Transl. Med.* **10**(12), 690. <https://doi.org/10.21037/atm-22-2135> (2022).
- Zhao, S. et al. Health study of 11,800 workers under occupational noise in Xinjiang. *BMC Public Health* **21**(1), 460. <https://doi.org/10.1186/s12889-021-10496-3> (2021).
- Wu, Y. et al. Combination of static and dynamic neural imaging features to distinguish sensorineural hearing loss: A machine learning study. *Front. Neurosci.* **18**, 1402039. <https://doi.org/10.3389/fnins.2024.1402039> (2024).
- Zhao, Y. et al. Machine learning models for the hearing impairment prediction in workers exposed to complex industrial noise: A pilot study. *Ear Hearing* **40**(3), 690–699. <https://doi.org/10.1097/AUD.0000000000000649> (2019).
- Abu Bakar, A. R., Lai, K. W. & Hamzaid, N. A. The emergence of machine learning in auditory neural impairment: A systematic review. *Neurosci. Lett.* **765**, 136250. <https://doi.org/10.1016/j.neulet.2021.136250> (2021).

7. Djemai, M. & Guerti, M. Kernel SVM classifiers based on fractal analysis for estimation of hearing loss. *ENPESJ* 2(1), 45–50. <https://doi.org/10.53907/enpesj.v2i1.88> (2022).
8. Park, K. V. et al. Machine learning models for predicting hearing prognosis in unilateral idiopathic sudden sensorineural hearing loss. *Clin. Exp. Otorhinol.* 13(2), 148–156. <https://doi.org/10.21053/ceo.2019.01858> (2020).
9. Aghakhani, A., Yousefi, M. & Yekaninejad, M. S. Machine learning models for predicting sudden sensorineural hearing loss outcome: A systematic review. *Ann. Oto. Rhinol. Laryn.* 133(3), 268–276. <https://doi.org/10.1177/00034894231206902> (2023).
10. Huang, R. et al. Assessment of brain function in patients with occupational noise-induced hearing loss by resting-state fMRI. *Chinese Imaging Journal of Integrated. Tradit. Western Med.* 21(2), 122–126. <https://doi.org/10.3969/j.issn.1672-0512.2023.02.005> (2023).
11. Huang, R. et al. Association functional MRI studies of resting-state amplitude of low frequency fluctuation and voxel-based morphometry in patients with occupational noise-induced hearing loss. *J. Occup. Environ. Med.* 62(7), 472–477. <https://doi.org/10.1097/JOM.0000000000001869> (2020).
12. Chen, J. et al. Altered brain activity and functional connectivity in unilateral sudden sensorineural hearing loss. *Neural. Plast.* 2020, 9460364. <https://doi.org/10.1155/2020/9460364> (2020).
13. Xu, X. M. et al. Sensorineural hearing loss and cognitive impairments: Contributions of thalamus using multiparametric MRI. *J. Magn. Reson. Imaging* 50(3), 787–797. <https://doi.org/10.1002/jmri.26665> (2019).
14. Li, Y., Wang, A., Huang, R., Li, L. & Xu, L. Regional homogeneity of brain function at rest in patients with occupational noise deaf. *Int. Med. Health Guidance News* 29(20), 2901–2905. <https://doi.org/10.3760/cma.j.issn.1007-1245.2023.20.016> (2023).
15. Luan, Y. et al. Abnormal functional connectivity and degree centrality in anterior cingulate cortex in patients with long-term sensorineural hearing loss. *Brain Imaging Behav.* 14(3), 682–695. <https://doi.org/10.1007/s11682-018-0004-0> (2020).
16. Wang, A. J. et al. Voxel-based morphometry (VBM) MRI analysis of gray matter in patients with occupational noise-induced hearing loss. *Zhonghua Lao Dong Wei Sheng Zhi Ye Bing Za Zhi* 36(9), 677–681. <https://doi.org/10.3760/cma.j.issn.1001-9391.2018.09.008> (2018).
17. Li, J. et al. Cortical thickness analysis and optimized voxel-based morphometry in children and adolescents with prelingually profound sensorineural hearing loss. *Brain Res.* 1430, 35–42. <https://doi.org/10.1016/j.brainres.2011.09.057> (2011).
18. Wang, R. Voxel-based morphology study in patients with sensorineural hearing loss. *Hebei Med. J.* 33(5), 663–665. <https://doi.org/10.3969/j.issn.1002-7386.2011.05.009> (2011).
19. Li, Y. et al. Cerebral cortex thickness in 55 patients with occupational noise deafness. *J. Pract. Med. Tech.* 30(9), 628–631. <https://doi.org/10.19522/j.cnki.1671-5098.2023.09.005> (2023).
20. Tan, L. et al. Combined analysis of sMRI and fMRI imaging data provides accurate disease markers for hearing impairment. *NeuroImage Clin.* 3, 416–428. <https://doi.org/10.1016/j.nicl.2013.09.008> (2013).
21. Bing, D. et al. Predicting the hearing outcome in sudden sensorineural hearing loss via machine learning models. *Clin. Otolaryngol.* 43(3), 868–874. <https://doi.org/10.1111/coa.13068> (2018).
22. Chen, F., Cao, Z., Grais, E. M. & Zhao, F. Contributions and limitations of using machine learning to predict noise-induced hearing loss. *Int. Arch. Occup. Environ. Health* 94(5), 1097–1111. <https://doi.org/10.1007/s00420-020-01648-w> (2021).
23. Li, H. et al. Identification of bipolar disorder using a combination of multimodality magnetic resonance imaging and machine learning techniques. *BMC Psychiatry* 20(1), 488. <https://doi.org/10.1186/s12888-020-02886-5> (2020).
24. GBZ 49-2014 Diagnosis of occupational noise-induced deafness. (2014). National occupational health standards of the People's Republic of China.
25. Yan, C. G., Wang, X. D., Zuo, X. N. & Zang, Y. F. DPABI: Data processing and analysis for (resting-state) brain imaging. *Neuroinformatics* 14(3), 339–351. <https://doi.org/10.1007/s12021-016-9299-4> (2016).
26. Destrieux, C., Fischl, B., Dale, A. & Halgren, E. Automatic parcellation of human cortical gyri and sulci using standard anatomical nomenclature. *NeuroImage* 53(1), 1–15. <https://doi.org/10.1016/j.neuroimage.2010.06.010> (2010).
27. Tibshirani, R. Regression shrinkage and selection via the lasso. *J. R. Stat. Soc. Ser. B (Methodol.)* 58(1), 267–288. <https://doi.org/10.1111/j.2517-6161.1996.tb02080.x> (1996).
28. Chang, C. & Lin, C. LIBSVM: A library for support vector machines. *ACM Trans. Intell. Syst. Technol.* <https://doi.org/10.1145/1961189.1961199> (2011).
29. Breiman, L. Random forests. *Mach. Learn.* 45, 5–32. <https://doi.org/10.1023/A:1010933404324> (2001).
30. Liu, L. et al. Abnormal regional signal in the left cerebellum as a potential neuroimaging biomarker of sudden sensorineural hearing loss. *Front. Psychiatry* 13, 967391. <https://doi.org/10.3389/fpsy.2022.967391> (2022).
31. Wei, X. et al. Auxiliary diagnosis models of bipolar disorder based on functional magnetic resonance imaging and deep learning. *Chin. J. Psychiatry* 55(1), 30–37. <https://doi.org/10.3760/cma.j.cn113661-20210430-00147> (2022).
32. Zou, Q. H. et al. An improved approach to detection of amplitude of low-frequency fluctuation (ALFF) for resting-state fMRI: fractional ALFF. *J. Neurosci. Methods* 172(1), 137–141. <https://doi.org/10.1016/j.jneumeth.2008.04.012> (2008).
33. Zang, Y., Jiang, T., Lu, Y., He, Y. & Tian, L. Regional homogeneity approach to fMRI data analysis. *NeuroImage* 22(1), 394–400. <https://doi.org/10.1016/j.neuroimage.2003.12.030> (2004).
34. Zuo, X. N. et al. Network centrality in the human functional connectome. *CEREB CORTEX* 22(8), 1862–1875. <https://doi.org/10.1093/cercor/bhr269> (2011).
35. Huang, F. F. et al. Functional and structural MRI based obsessive-compulsive disorder diagnosis using machine learning methods. *BMC Psychiatry* 23(1), 792. <https://doi.org/10.1186/s12888-023-05299-2> (2023).
36. Li, P., Huang, L., Wang, C., Li, C. & Lai, J. Brain network analysis for auditory disease: A twofold study. *Neurocomputing* 347, 230–239. <https://doi.org/10.1016/j.neucom.2019.04.013> (2019).
37. Yang, T. et al. Altered regional activity and connectivity of functional brain networks in congenital unilateral conductive hearing loss. *NeuroImage Clin.* 32, 102819. <https://doi.org/10.1016/j.nicl.2021.102819> (2021).
38. Cao, W. & Guan, B. Voxel-based morphometry study of the brain structures in patients with congenital hereditary hearing loss. *Zhonghua Er Bi Yan Hou Tou Jing Wai Ke Za Zhi* 55(2), 81–86. <https://doi.org/10.3760/cma.j.issn.1673-0860.2020.02.001> (2020).
39. Guo, P. et al. Alterations of regional homogeneity in children with congenital sensorineural hearing loss: A resting-state fMRI study. *Front. Neurosci.* 15, 678910. <https://doi.org/10.3389/fnins.2021.678910> (2021).
40. Li, J. et al. Altered static and dynamic intrinsic brain activity in unilateral sudden sensorineural hearing loss. *Front. Neurosci.* 17, 1257729. <https://doi.org/10.3389/fnins.2023.1257729> (2023).
41. Li, Y. T. et al. Dynamic alterations of functional connectivity and amplitude of low-frequency fluctuations in patients with unilateral sudden sensorineural hearing loss. *Neurosci. Lett.* 772, 136470. <https://doi.org/10.1016/j.neulet.2022.136470> (2022).
42. Shiell, M. M., Champoux, F. & Zatorre, R. J. Reorganization of auditory cortex in early-deaf people: Functional connectivity and relationship to hearing aid use. *J. Cogn. Neurosci.* 27(1), 150–163. https://doi.org/10.1162/jocn_a_00683 (2015).
43. Wolak, T. et al. Altered functional connectivity in patients with sloping sensorineural hearing loss. *Front. Hum. Neurosci.* 13, 284. <https://doi.org/10.3389/fnhum.2019.00284> (2019).

Author contributions

Lv Minghui: Data curation; investigation; methodology; project administration; writing - original draft; writing - review and editing. Wang Liping: Data curation; investigation; Visualization; software. Huang Ranran: Data curation; writing - original draft. Wang Aijie: Data curation; software. Li Yunxin: Data curation. Zhang Guowei: Formal analysis; funding acquisition; supervision.

Competing interests

The authors declare no competing interests.

Ethical approval

Written informed consent was obtained from all participants after a full explanation of the procedures involved. This study protocol was approved by the Yantaishan Hospital Ethics Committee. The ethics approval number (2023014) and ethical approval date is february 24, 2023. All methods were performed in accordance with the relevant guidelines and regulations.

Additional information

Correspondence and requests for materials should be addressed to G.Z.

Reprints and permissions information is available at www.nature.com/reprints.

Publisher's note Springer Nature remains neutral with regard to jurisdictional claims in published maps and institutional affiliations.

Open Access This article is licensed under a Creative Commons Attribution-NonCommercial-NoDerivatives 4.0 International License, which permits any non-commercial use, sharing, distribution and reproduction in any medium or format, as long as you give appropriate credit to the original author(s) and the source, provide a link to the Creative Commons licence, and indicate if you modified the licensed material. You do not have permission under this licence to share adapted material derived from this article or parts of it. The images or other third party material in this article are included in the article's Creative Commons licence, unless indicated otherwise in a credit line to the material. If material is not included in the article's Creative Commons licence and your intended use is not permitted by statutory regulation or exceeds the permitted use, you will need to obtain permission directly from the copyright holder. To view a copy of this licence, visit <http://creativecommons.org/licenses/by-nc-nd/4.0/>.

© The Author(s) 2025